Journal of Zhejiang University-SCIENCE B (Biomedicine & Biotechnology) in press
www.jzus.zju.edu.cn; www.springer.com/journal/11585
E-mail: jzus_b@zju.edu.cn

Research Article

https://doi.org/10.1631/jzus.B2500142

Momordicine I induces ER stress and inhibits OSCC by targeting ribosomal proteins

Jianlu KONG[1*], Ziyu ZHU[1*], Yijie HU[1], Siyi ZHOU[1], Tianyi GU[1], Xiao SHEN[2], Huiming WANG[1✉], Mengfei YU[1], Yu LIU[1✉]

[1]*Stomatology Hospital, School of Stomatology, Zhejiang University School of Medicine, Zhejiang Provincial Clinical Research Center for Oral Diseases, Key Laboratory of Oral Biomedical Research of Zhejiang Province, Cancer Center of Zhejiang University, Hangzhou 310006, China*
[2]*The Second School of Clinical Medicine, Zhejiang Chinese Medical University, Hangzhou 310053, China*

Abstract: Oral squamous cell carcinoma (OSCC) is one of the most common malignant tumors worldwide. This necessitates the development of innovative drugs with high efficiency, low toxicity, and good tolerance. Bitter melon extract has been reported to have potent anticancer activity against OSCC. We evaluated the effects of nine triterpenoids from bitter melon extract on OSCC using CCK8 proliferation and Transwell migration assays. Among the nine triterpenoids, momordicine I (MI) exhibited the strongest anticancer activity against OSCC. Animal experiments also showed that MI inhibited OSCC cell growth in vivo. Additionally, MI decreased the mitochondrial membrane potential and promoted apoptosis in OSCC. RNA-seq analysis revealed that MI induced an unfolded protein response (UPR) and endoplasmic reticulum (ER) stress, which was confirmed by western blotting and RT-qPCR. Cellular thermal shift assay (CETSA) and mass spectrometry (MS) analysis, combined with molecular docking, identified ribosomal proteins (RPL7, RPL11, RPL12, RPL18, RPL30, RPL38, RPS13, RPS25) as MI targets. By targeting ribosomal proteins, MI likely disrupts ribosome-mediated protein folding, leading to UPR and ER stress. In summary, MI targets ribosomal proteins to induce ER stress and inhibit OSCC, highlighting its therapeutic potential.

Key words: Oral squamous cell carcinoma (OSCC); Momordicine I (MI); Endoplasmic Reticulum (ER) stress; Ribosomal proteins

unedited

1 Introduction

Oral cancer is a malignant tumor with the highest incidence rate among tumors worldwide, with an annual incidence of 354 864 and a mortality of 177 384 (Bray et al., 2018). About 90% of these cancers are oral squamous cell carcinomas (OSCC) (Feller et al., 2013; Dai et al., 2023). The most common risk factors for OSCC are tobacco and alcohol use (Blot et al., 1988), betel nut chewing (Chen et al., 2008), and human papilloma virus (HPV) infection (Hennessey et al., 2009). Although standard treatment is a combination of surgery, radiation, and chemotherapy, the five-year survival rate of OSCC is only about 50% (Bray et al., 2018; Chen et al., 2018b). New drugs with high efficiency, low toxicity, and good tolerance are urgently needed to improve treatment outcomes and reduce costs. Treatment with natural phytochemical compounds is an emerging strategy to prevent, impede, or cure cancer (Wang et al., 2012; Gao et al., 2023). Bitter melon is rich in bioactive

✉ Yu LIU, 7514061@zju.edu.cn
Huiming WANG, whmwhm@zju.edu.cn
* The two authors contributed equally to this work
Jianlu KONG, https://orcid.org/0000-0002-9264-2929
Ziyu ZHU, https://orcid.org/0000-0001-7680-5292
Huiming WANG, https://orcid.org/0000-0002-1131-7455
Yu LIU, https://orcid.org/0000-0003-3699-4759

Received Mar. 25, 2025; Revision accepted Sept. 10, 2025;
Crosschecked xxx. xx, 20xx; Published online xxx. xx, 20xx

© Zhejiang University Press 2025

chemical components such as cucurbitane-type tetracyclic triterpenoids, triterpenoid glycosides, phenolic acid flavones, essential oils, saponins, fatty acids, and proteins (Chen et al., 2021). In recent years, studies have suggested the potent antitumor properties of bitter melon extract in OSCC (Sur and Ray, 2021; Yang et al., 2021). However, the detailed mechanism by which bitter melon extract inhibits OSCC has not been fully clarified. Triterpenoids from bitter melon extract have shown anticancer activity in breast cancer cells (Bai et al., 2016), prostate cancer cells (Pitchakarn et al., 2012), ovarian cancer cells (Pitchakarn et al., 2017) and hepatoma cells (Yue et al., 2019).

Momordicine I (MI), a triterpenoid monomer compound from bitter melon extract, has recently been reported to have an anticancer effect on OSCC and head and neck cancer (HNC) (Sur et al., 2021). The study showed that MI displayed antitumor activity in HNC, possibly through the c-Met pathway. The bioactive metabolite from bitter melon extract was identified and MI was found to be a potent anticancer component of bitter melon extract. However, the study did not compare the anticancer effect of MI with that of other bitter melon triterpenoid monomer compounds that might also play an anticancer role in HNC. (Sur et al., 2024) revealed that MI suppressed HNC growth by reprogramming the immunosuppressive effect of tumor-infiltrating macrophages and B lymphocytes. (Lee et al., 2022) used ultrasound- and microwave-assisted methods to extract triterpenoids from bitter melon extract and found MI to be one of the most abundant triterpenoid compounds. (Lee, et al., 2022) also showed that MI had a better proliferation-inhibitory effect on OSCC cells than other bitter melon triterpenoid monomers, 3β, 7β, 25-Trihydroxycucurbita-5, 23(E)-dien-19-al . A recent study showed that MI suppressed glioma growth by promoting apoptosis and impairing mitochondrial oxidative phosphorylation (Kao et al., 2023). However, these studies did not fully elucidate the molecular mechanisms underlying MI's anticancer role. Specifically, the direct targets of MI remain unidentified, and the transcriptomic impact of MI was not analyzed. Our research addressed these gaps by identifying ribosomal proteins as direct targets of MI and showing that MI induces endoplasmic reticulum (ER) stress to inhibit OSCC.

unedited

2 Materials and methods

2.1 Cells

OSCC cell lines CAL27 and HN4 (RRID:CVCL_IS30) were used in this study. The cells were cultured in Dulbecco's modified Eagle's medium (DMEM; SH30243.01, HyClone, USA) supplemented with 10% (v/v) fetal bovine serum (FBS; Life Technologies, Gibco, USA) and 1% (v/v) penicillin/streptomycin solution (10378016, Gibco, USA). The cultures were maintained at 37 °C in a 5% CO_2 incubator and observed daily using an inverted microscope. Subculturing was performed using 0.25% (w/v) trypsin-EDTA when the cells reached 70%–80% confluency.

2.2 Monomer compounds from bitter melon and ER stress inhibitor

MI (ChemFaces, CFN92076) was dissolved in dimethyl sulfoxide (DMSO, MedChemExpress, HY-Y0320) at a concentration of 50 mmol/L. In most experiments in this study, MI was used at a concentration of 25 μmol/L to treat OSCC cells. Typically, 1 μL of MI (50 mmol/L) was added to 2 mL of culture medium to achieve a final concentration of 25 μmol/L, whereas 1 μL of DMSO was added to 2 mL of culture medium for the control group. Additionally, other compounds such as momodicine II (MII; ChemFaces, CFN95167), momodicine V (MV; ChemFaces, CFN95164), momodicoside L (MSL; ChemFaces, CFN92307), momodicoside X (MSX; ChemFaces, CFN95170), momodicoside K (MSK; ChemFaces, CFN92305), Kuguacin J (KJ; ChemFaces, CFN92073), Kuguacin N (KN; ChemFaces, CFN92074), and Kuguaglycoside C (KSC; ChemFaces, CFN92309) were prepared in DMSO at a concentration of 50 mmol/L. ER stress inhibitor tauroursodeoxycholic acid (TUDCA; MedChemExpress, HY-19696) was prepared in DMSO at a concentration of 200 mmol/L.

2.3 Cell proliferation and migration assay

CAL27 and HN4 cells were seeded in 96-well plates at 2 000 cells per well. After 24 h of incubation, the medium was replaced with a CCK-8 mixture (1:10 ratio of CCK8 to medium; Beyotime Biotechnology, Shanghai, China). Absorbance at 490 nm was measured using a microplate reader (Synergy H1, BioTek, USA) at 24, 48, and 72 h.

Cell migration was assessed using a Transwell system (140644, Thermo Scientific, USA). A total of 1 × 105 cells were seeded in the upper chamber with serum-free medium, while the lower chamber contained 10% FBS as a chemoattractant. After 24 h at 37 °C, non-migrated cells on the upper surface were removed, and migrated cells on the lower surface were fixed with 4% paraformaldehyde and stained with 0.1% crystal violet. Images were captured at 4× magnification using an optical microscope (Olympus, Tokyo, Japan). The crystal violet was dissolved in 33% acetic acid, and absorbance was measured at 570 nm using a microplate reader (Synergy H1, BioTek, USA).

2.4 Spheroid culture experiments

CAL27 cells were inoculated into 96-well microplates (Corning, USA) at a density of 10 000 cells per well to form spheroids. After 24 h of incubation, a photo of the spheroids was taken under the microscope and recorded as time 0. The 96 wells were divided into two groups: DMSO and MI. The MI group was treated with 100 μM of MI. The DMSO group was treated with an equal amount of DMSO to form a control group. Images were taken under a microscope 48 h later.

2.5 RT‐qPCR

Total RNA from cultured cells was isolated using Trizol (Invitrogen, Carlsbad, CA, USA), and real-time quantitative polymerase chain reaction (RT-qPCR) experiments were conducted with Takara (Dalian, China) reagents (RR047A and DRR820A) according to the manufacturer's instructions. RT-qPCR reactions were performed using the Bio-Rad CFX384™ Real Time System (Bio-Rad CFX Maestro). The sequences of the primers used are listed in Supporting Information Table S1. The housekeeping gene GAPDH was used as a standard reference gene to analyze the expression levels of the target genes.

2.6 Western blots

Cells were lysed in RIPA reagent (Applygen, Beijing, China) supplemented with 1% protease inhibitor and 1% phosphatase inhibitor to isolate the total protein. The primary antibodies used were PUMA (1:1000, ab9645, Abcam, USA, RRID: AB_1151444), β-actin (1:1000, GB15003, Servicebio, China), GRP78 (1:1000, ab21685, Abcam, USA), and EIF2ak3 (1:1000, 205364-T38, Sino Biological, Beijing, China). Each blot was re-probed with anti-rabbit antibody (Dawen Biotec, Hangzhou, China, 1:3000). Immunoreactive proteins were detected using the Pierce ECL Western Blot Substrate Kit (Thermo Fisher Scientific, USA) and band intensities were quantified using Image Lab software (Bio-Rad, USA).

2.7 Immunofluorescence

Four percent paraformaldehyde was used to immobilize CAL27 cells in a six-well plate for 15 min. Subsequently, 0.5% Triton X-100 (Sigma Aldrich) prepared with phosphate-buffered saline (PBS, Sigma Aldrich) was used to treat the samples at room temperature for 15 min to permeabilize the cell membrane. After sealing the samples with 5% bovine serum albumin (BSA, Sigma Aldrich) prepared with PBS for 30 min, primary antibodies were added and incubated at 4 °C overnight. The fluorescent secondary antibodies were incubated in the dark for 30 min. Finally, the cytoskeleton was stained with ActinTracker Red-555 (1:200; Beyotime, Shanghai, China) and the nucleus with an antifade mounting solution containing DAPI (C1211, Applygen, Beijing, China). Confocal laser scanning microscopy (Leica TCS SP8, Germany) was used to observe the corresponding protein localization.

unedited

In a separate procedure, 4% paraformaldehyde was used to immobilize cells cultured on slides in 24-well plates for 15 min. Next, 0.5% Triton X-100, prepared with PBS, was used to treat the samples at room temperature for 15 min to permeabilize the cell membrane. After sealing the samples with 5% BSA prepared with PBS for 30 min, the primary antibody was added and incubated at 4 °C overnight. The fluorescent secondary antibodies were incubated in the dark for 30 min. Nuclei were stained with DAPI. Between steps involving different reagents, the cells on the slides were washed three times in PBS for 5 min each, with 500 μl of each reagent used per well. After mounting, the slides were observed under a confocal laser scanning microscope (Leica TCS SP8, Germany). Antibodies against GRP78 (1:200, ab21685, Abcam, USA) and α-tubulin (1:200, F2168, Cell Signaling Technology, USA) were used.

2.8 RNA-seq analysis

OSCC CAL27 cells treated with MI and DMSO were designated as the MI group (experimental group) and DMSO group (control group). In the MI group, OSCC cells were treated with 25 μM of MI for 48 h. In the DMSO group, cells were treated with DMSO for 48 h. To achieve a 25 μM concentration in the MI group, 1 ul of MI (50 mM in DMSO) was added to 2 ml culture medium, and for the control group, 1ul DMSO was added to 2 ml culture medium. The MI and DMSO groups were cultured in a 6-well plate with three replicate wells.

2.9 Cellular thermal shift assay (CETSA)

OSCC CAL27 cells were cultured in 10-cm dishes and reached over 95% confluence with a cell number of about 2×10^7. In the MI group, MI was added to a final concentration of 25 μM and incubated for 80 min at 37 °C with 5% CO_2. In the DMSO group, cells were treated with the same amount of DMSO. After that, the cells were collected and resuspended to 3×10^6 cells/100 ul in PBS supplemented with protease complete (Roche) and phosphatase PhosSTOP inhibitors (Roche). The cell suspension was then aliquoted into 200-ul tubes, with 100 ul in each sample. In our CETSA experiment, samples were heated to 50 °C or temperature gradients (40, 45, 50, 55, 60 °C) in a Life Touch thermal cycler (Bioer Technology, Hangzhou, China) for 3 min, cooled for 3 min at RT, and then lysed by three freeze-thaw cycles using liquid nitrogen. Finally, the samples were centrifuged at 15,000g for 45 min at 4 °C. The supernatant was then transferred to a new tube for further MS assays or western blotting.

2.10 Molecular docking

The compound structure of MI was retrieved from the PubChem database (https://pubchem.ncbi.nlm.nih.gov/) and the crystal structures of the target protein were downloaded from the Protein Data Bank (PDB) (https://www.rcsb.org/). They were RPL7 (PDB ID:8GLP), RPL11 (PDB ID:4XXB), RPL12 (PDB ID:8FKV), RPS13 (PDB ID:8GLP), RPL18(PDB ID:8GLP), RPS25 (PDB ID:8GLP), RPL30 (PDB ID:3VI6), and RPL38 (PDB ID:8GLP). The processing and optimization of molecular docking were accomplished using the Glide module in Schrödinger Maestro software. Protein processing was performed using the Protein Preparation Wizard module, and molecular docking was performed using the Standard Precision Glide Docking method.

2.11 Animal experiments

All animal experiments were performed in accordance with the protocol approved by the Animal Care and Use Committee of Zhejiang University. Ten male BALB/c nude mice, aged 6 weeks (Charles River, China), were divided into two groups with five animals in each group. The mice were reared under SPF conditions throughout the entire process. A total of 5×10^6 cells were injected subcutaneously into the mice. Two days after cell injection, Momordicine I (ChemFaces, CFN92076) was intraperitoneally injected into the experimental group (MI group) every other day at a dose of 30 mg/kg. The control group (DMSO group) received intraperitoneal injection of an equal volume of solvent containing an equivalent amount of DMSO. Tumor fluorescence

unrevised

was observed weekly using the IVIS Lumina III (PerkinElmer, USA) after intraperitoneal injection of D-Luciferin Sodium Salt (GM-040611, Genomeditech, China, 15 mg/mL, 200 μl per animal). Fluorescence was quantified using Living Image Analysis software (PerkinElmer, USA). After 4 weeks of continuous monitoring, the animals were euthanized and tumor tissues were harvested for photographic documentation and weight measurement.

2.12 Surface plasmon resonance (SPR)

SPR experiments were performed at 25 °C using a Biacore 8K (Cytiva). The running buffer consisted of 10 mM phosphate buffer, pH 7.4, 150 mM NaCl, 5% DMSO and 0.05% Tween 20. The Biacore Insight evaluation software 5.0 (Cytiva) was used for data analysis. All sensorgrams were reference and blank subtracted. Running buffer was used for blank injections, and bulk effects were corrected using solvent correction. Proteins RPL11 (FineTest, P2767), RPL12 (FineTest, P5056), RPL38 (FineTest, P1082) and RPS13 (FineTest, P5493) were immobilized on a CM5 sensor chip using standard amine coupling. For the interaction studies, small molecule MI was dissolved in running buffer and injected in a 2-fold dilution concentration series ranging from 0.19 to 12.5 μM. The association was followed for 100 s and the dissociation for 150 s. Before and after every concentration series, a blank was injected. The steady-state values were calculated from the sensorgrams and plotted against the concentration. The data were fitted to a single-site binding model to calculate KD.

2.13 *RPL7* and *RPL11* knockdown by siRNAs

Three siRNAs targeting *RPL7* and three targeting *RPL11* were purchased from Tsingke Biotechnology. The detailed sequences are shown in Table S2. The siRNAs were transfected using the GenMute™ siRNA Transfection Reagent from SignaGen Laboratories. Transfection efficiency was assessed after 48 h, and the siRNA with the highest interference efficiency for *RPL7* (*RPL7*si1) as well as the siRNA with the highest interference efficiency for *RPL11* (*RPL11*si1) were selected for downstream experiments. MI treatment was added 24 h post-transfection for subsequent detection of internal and external markers and cell proliferation assays.

2.14 Statistical process

The results are presented as mean ± standard deviation. The Student's t-test (two groups: unpaired; tails: two-tailed) was used to calculate the p-values of the results. All groups (minimum n=3) were tested for normality using Shapiro-Wilk tests and for homoscedasticity using F-tests (for two-group comparisons) or Brown-Forsythe tests (for multi-group comparisons) (Table S3). For data meeting both assumptions, we applied Student's t-test for two-group comparisons; for unequal variances, logarithmic transformation was performed, followed by retesting. If variances remained unequal, Welch's corrected t-test was used. In two-factor analyses, we assessed normality with Shapiro-Wilk tests and homoscedasticity with Brown-Forsythe tests, then performed two-way ANOVA. All experiments were carried out at least three times or performed in triplicate, and representative data are shown. All p-values are two-tailed, and p-values less than 0.05 are considered statistically significant.

3 Results

3.1 The inhibition of OSCC cell proliferation and migration by MI

Bitter melon extract has been reported to have an obvious antitumor effect in OSCC. Tetracyclic triterpenoids are a class of compounds known for their anticancer effects. Unlike previous studies on the role of MI in OSCC, our study identified the key triterpenoid monomer compound that inhibits OSCC. We compared the effects of nine commercially available bitter melon triterpenoid monomer compounds: momodicine I (MI), momodicine II (MII), momodicine V (MV), momodicoside L (MSL), momodicoside X (MSX), momodicoside K (MSK), Kuguacin J (KJ), kuguacin (KN), and Kuguaglycoside C (KSC). We selected and purchased nine

unedited

common tetracyclic triterpenoid monomers from bitter melon extract: MI, MII, MV, MSL, MSX, MSK, KJ, and KN. We used the CCK8 and Transwell migration assays to identify the most potent anticancer monomer compound among the nine common tetracyclic triterpenoids in the extract. The IC50 of MI against CAL27 cells after 48-h treatment was about 25 μM (Fig. S1). Therefore, 25 μM was used as a sole treatment concentration in most experiments. To ensure comparable results, tetracyclic triterpenoids were tested at a uniform concentration of 25 μM. The CCK8 assay revealed that MI had the strongest inhibitory effect on the proliferation of the OSCC cell lines CAL27 and HN4 among the nine tetracyclic triterpenoids from the bitter melon extract (Figs. 1a and 1b). The Transwell migration assay also indicated that MI had the strongest inhibitory effect on the migration of OSCC cell lines CAL27 and HN4 among the nine tetracyclic triterpenoids from the bitter melon extract (Figs. 1c-f).

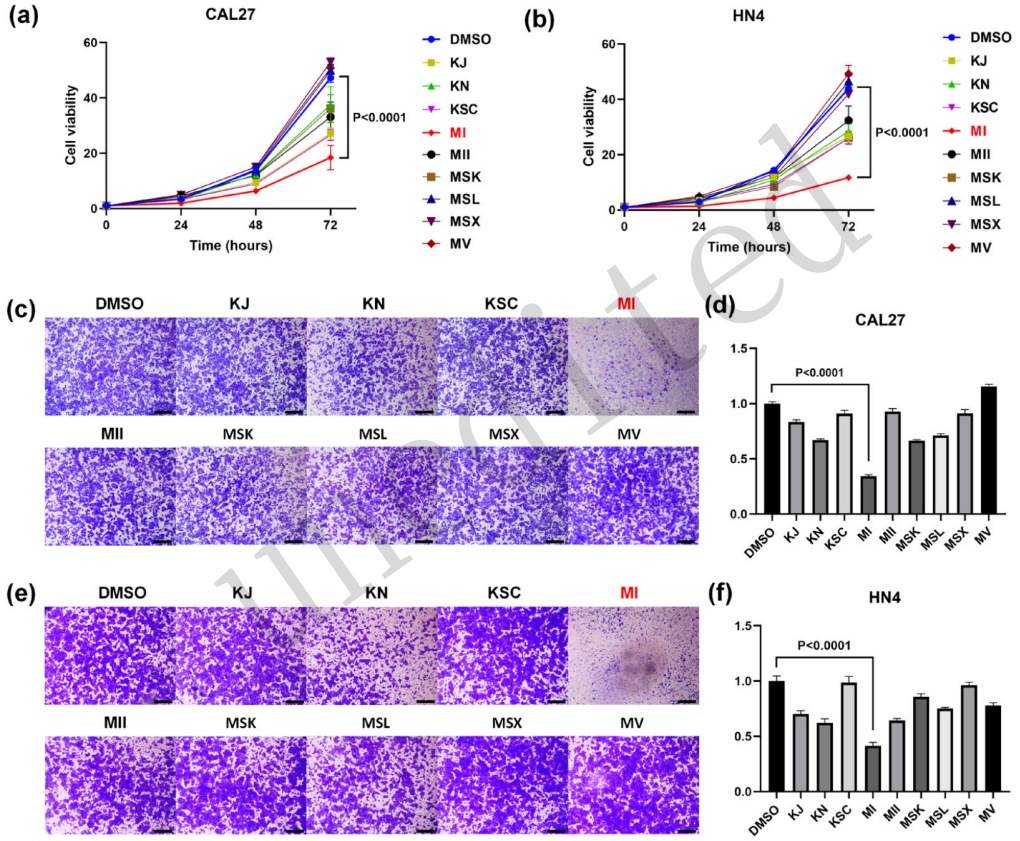

Fig. 1 MI-induced inhibition of OSCC cell growth in vitro. (a) The CCK8 assay showed that MI strongly inhibited OSCC cell CAL27 proliferation among the nine triterpenoids from bitter melon extract. CAL27 cells were treated with different triterpenoids from the bitter melon extract at a concentration of 25 μM. Data are represented as mean±standard deviation (SD), n=3. (b) The CCK8 assay showed that MI strongly inhibited HN4 proliferation in OSCC cells among the nine triterpenoids from bitter melon extract. HN4 was treated with different triterpenoids from the bitter melon extract at a concentration of 25 μM. Data are represented as mean±standard deviation (SD), n=3. (c) Transwell assay showed that MI strongly inhibited OSCC cell CAL27 migration among the nine triterpenoids from bitter melon extract. CAL27 cells were treated with different triterpenoids from the bitter melon extract at a concentration of 25 μM. The scale bar represents 500 μm. (d) The histogram shows the quantification of the Transwell assay of OSCC CAL27 cells treated with nine triterpenoids. Data are represented as mean±standard deviation (SD), n=3. (e) Transwell assay showed that MI strongly inhibited OSCC cell HN4 migration among the nine triterpenoids from bitter melon extract. HN4 was treated with different triterpenoids from the bitter melon extract at a concentration of 25 μM. The scale bar represents 500 μm. (f) The histogram shows the quantification of the Transwell assay of OSCC cell HN4 treated with nine triterpenoids. Data are represented as mean±standard deviation (SD), n=3.

Uncorrected

3.2 The inhibition of OSCC cell growth in vivo and promotion of apoptosis by MI

Similar to earlier studies, we elucidated the inhibitory effect of MI on OSCC both in vitro and in vivo. In vitro experiments, including CCK8 and Transwell migration assays, showed that MI significantly inhibited the proliferation and migration of OSCC cells among the nine tetracyclic triterpenoids derived from the bitter melon extract. We then used a subcutaneous tumor formation model in nude mice to confirm the anticancer effects of MI on OSCC in vivo. About four days after injecting OSCC cells into nude mice for subcutaneous tumorigenesis, a visible tumor mass was formed. Ten mice were randomly divided into two groups. In the experimental group, we administered MI (30 mg/kg/mouse) via intraperitoneal injection into nude mice once daily. We referred to the dosage of MI in mice in another article (Sur, et al., 2021). In the control group, an equal volume of solvent containing an equivalent amount of DMSO was injected daily. When we first injected into nude mice, we used a small-animal imaging system to detect tumor fluorescence signals in advance (Fig. 2a). We then detected the tumor fluorescence signals weekly using a small-animal imaging system. After four weeks of MI treatment, the mice were imaged, revealing that the fluorescence signal of the tumors in the experimental group treated with MI was significantly lower than that in the control group (Figs. 2b and 2c). Following four weeks of MI treatment and fluorescence signal detection, mice were euthanized. The weight of the xenograft tumors in the MI-treated experimental group was significantly lower than that of those in the control group (Figs. 2d and 2e). These data indicate that MI significantly inhibited the growth of OSCC cells in vivo, demonstrating its potent anticancer effect on OSCC. During the animal experiment, we also measured changes in the body weight of the mice. No significant changes in body weight were observed in the mice after MI treatment (Fig. S2a). To further detect the in vivo toxicity of MI, we administered the same dosage as in the original experiment to both the experimental and control groups of nude mice for one week and tested the liver and kidney function indicators. No significant differences were found between the groups (Figs. S2b-2g). Additionally, in the spheroid culture experiments, the experimental group (DMSO) and the control group (MI) each contained three replicate spheroids. A significant inhibitory effect on the growth of spheroids derived from the OSCC cell line CAL27 was observed (Figs. 2f and 2g), suggesting that MI has the potential to inhibit the growth of OSCC cell-derived spheroids.

With evidence of anticancer effects of MI on OSCC both in vitro and in vivo, we further investigated its impact on apoptosis in OSCC cells. A decline in the mitochondrial transmembrane potential is a key indicator of apoptosis. We used the JC-1 assay to measure mitochondrial membrane potential. Treatment with 25 μM MI for 48 h significantly reduced the mitochondrial membrane potential in the OSCC cell line CAL27 compared to that of the control group (Figs. 2h and 2i). The effect of MI on OSCC cell apoptosis was analyzed using flow cytometry (FCM). The apoptosis rate increased in OSCC cells treated with 25 μM MI for either 24 or 48 h when compared to the control group (Figs. 2j and 2k).

Unedited

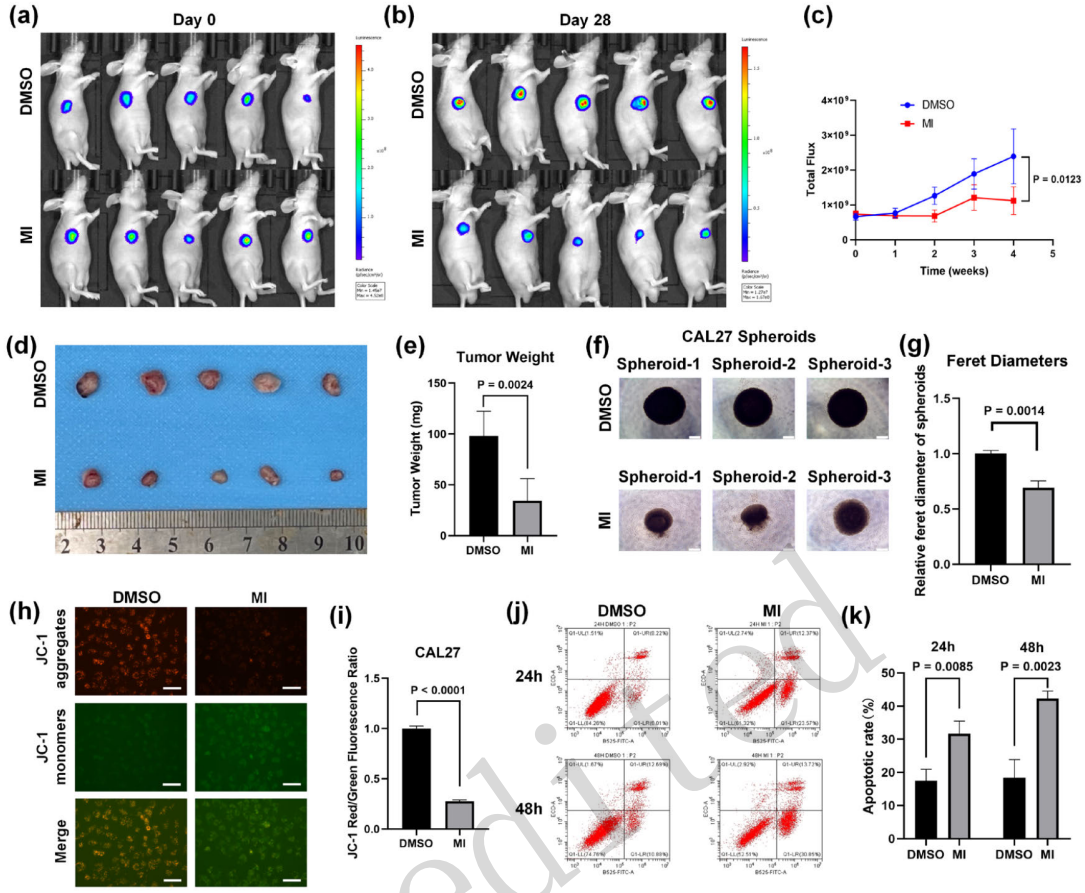

Fig. 2 The inhibition of OSCC cell growth in vivo and promotion of apoptosis by MI. (a) Representative images of luciferase signals of subcutaneous tumorigenesis in nude mice using IVIS® Spectrum at Day 0. A total of 5 × 10^6 cells were subcutaneously injected into each mouse. Day 0 was the starting day when MI (30 mg/kg) or the isovolumetric solvent DMSO was injected into nude mice. MI and DMSO represent the groups injected with MI (30 mg/kg) or the isovolumetric solvent DMSO, respectively. (b) Representative images of luciferase signals of subcutaneous tumorigenesis in nude mice using IVIS® Spectrum at Day 28. Day 28 indicated the 28th day after CAL27 cells were injected subcutaneously. MI or DMSO refers to the group injected with MI (30 mg/kg) or the isovolumetric solvent DMSO, respectively. (c) Quantification of the photon flux from subcutaneous tumorigenesis in nude mice. Data are represented as mean±standard deviation (SD), n=5. (d) Representative images of subcutaneous tumorigenesis in nude mice. (e) Histogram of tumor weight from subcutaneous tumorigenesis in nude mice. The weight of tumors from subcutaneous tumorigenesis in nude mice treated with MI was significantly lower than that of tumors in mice of the control group treated with DMSO. Data are represented as mean±standard deviation (SD), n=5. (f) The effect of MI (100 μM) on the growth of spheroids of OSCC cells CAL27 after 48 h. MI significantly inhibited the growth of spheroids of OSCC cells CAL27. The scale bar represents 500 μm. (g) Quantification of Feret diameters of spheroids (Fig. 2f). Data are represented as mean±standard deviation (SD), n=3. (h) JC-1 staining showed that mitochondrial membrane potential was down-regulated in OSCC cell CAL27 treated with MI (25 μM) for 48 h. The scale bar represents 100 μm. (i) Quantification of the JC-1 Red/Green fluorescence ratio in Fig. 2g shows a significant decrease in the mitochondrial membrane potential of OSCC cells CAL27 treated with MI. The scale bar represents 100 μm. Data are represented as mean±standard deviation (SD), n=3. (j) Flow cytometry assay showing that apoptosis was induced in OSCC cell CAL27 treated with MI (25 μM) for 24 h and 48 h. Data are represented as mean±standard deviation (SD), n=3. (k) Quantification of the apoptotic rate shown in Fig. 2j indicates a significant increase in apoptosis in OSCC cells CAL27 treated with MI (25 μM) for both 24 h and 48 h. Data are represented as mean±standard deviation (SD), n=3.

3.3 The induction of ER stress in OSCC cells by MI

Our comparative analysis showed that MI was the most potent anticancer triterpenoid monomer compound against OSCC among the nine compounds isolated from bitter melon extract. This finding piqued our interest in elucidating the detailed mechanism underlying the anticancer activity of MI in OSCC. In our previous study, we

Unedited

confirmed the inhibitory effects of MI on OSCC, both in vitro and in vivo. Based on these findings, we conducted RNA-seq analysis to investigate the signaling pathways affected by MI in OSCC cells. We treated the OSCC cell line CAL27 with 25 μM MI for 48 h to create the experimental group (MI group) and used the same cell line treated with an equivalent solvent DMSO as the control group (DMSO group). The results showed there were 2 298 differentially expressed genes between the MI and DMSO groups. Compared with the DMSO group, 940 genes were upregulated and 1 358 genes were downregulated in the MI group (Figs. 3a and 3c). We used DAVID Bioinformatics Resources to perform gene ontology (GO) analysis of the 940 upregulated genes in the MI group. The results indicated that these genes were significantly enriched in pathways associated with ER stress (Fig. 3b). To confirm the RNA-seq findings, we measured the levels of ER stress markers GRP78, PERK, and PUMA in CAL27 cells treated with 25 μM MI at various time points (24 h, 48 h, and 72 h) using western blot and RT-qPCR techniques. The results showed that the ER stress markers GRP78, PERK, and PUMA were significantly upregulated in OSCC CAL27 cells after MI treatment (Figs. 3d and 3e). Immunofluorescence imaging also revealed that OSCC CAL27 cells treated with MI exhibited higher expression of GRP78, a hallmark ER stress marker, than the control group (Fig. 3f). Subsequent gene set enrichment analysis (GSEA) of the ER stress-associated gene subset from the GO analysis confirmed the statistical significance of this enrichment (Figs. S3a-3d). In addition to GO analysis, we performed Kyoto Encyclopedia of Genes and Genomes (KEGG) pathway analysis on these 940 upregulated differentially expressed genes, which revealed significant enrichment (14 genes) in the ER stress-related pathway "Protein processing in endoplasmic reticulum". A co-expression network was constructed using the GeneMANIA platform for these 14 genes. Network topology analysis identified GRP78 (HSPA5) as a prominent hub gene based on its central position and high connectivity within the network (Figs. S3e-3f). These data corroborated the RNA-seq and comprehensive analyses results, suggesting that MI induces ER stress in OSCC cells.

To experimentally validate the role of ER stress in MI-induced apoptosis, we pretreated OSCC cells with the ER stress inhibitor TUDCA (tauroursodeoxycholic acid). Our results showed that TUDCA pretreatment significantly inhibited MI-induced upregulation of ER stress markers GRP78 and PERK (Fig. S4a). Furthermore, TUDCA pretreatment partially rescued MI-induced mitochondrial membrane potential depolarization (detected by JC-1 staining) and reduced the apoptosis rate (measured by flow cytometry), showing that ER stress plays a crucial role in mediating MI-induced apoptosis in OSCC cells (Figs. S4b-4h).

unedited

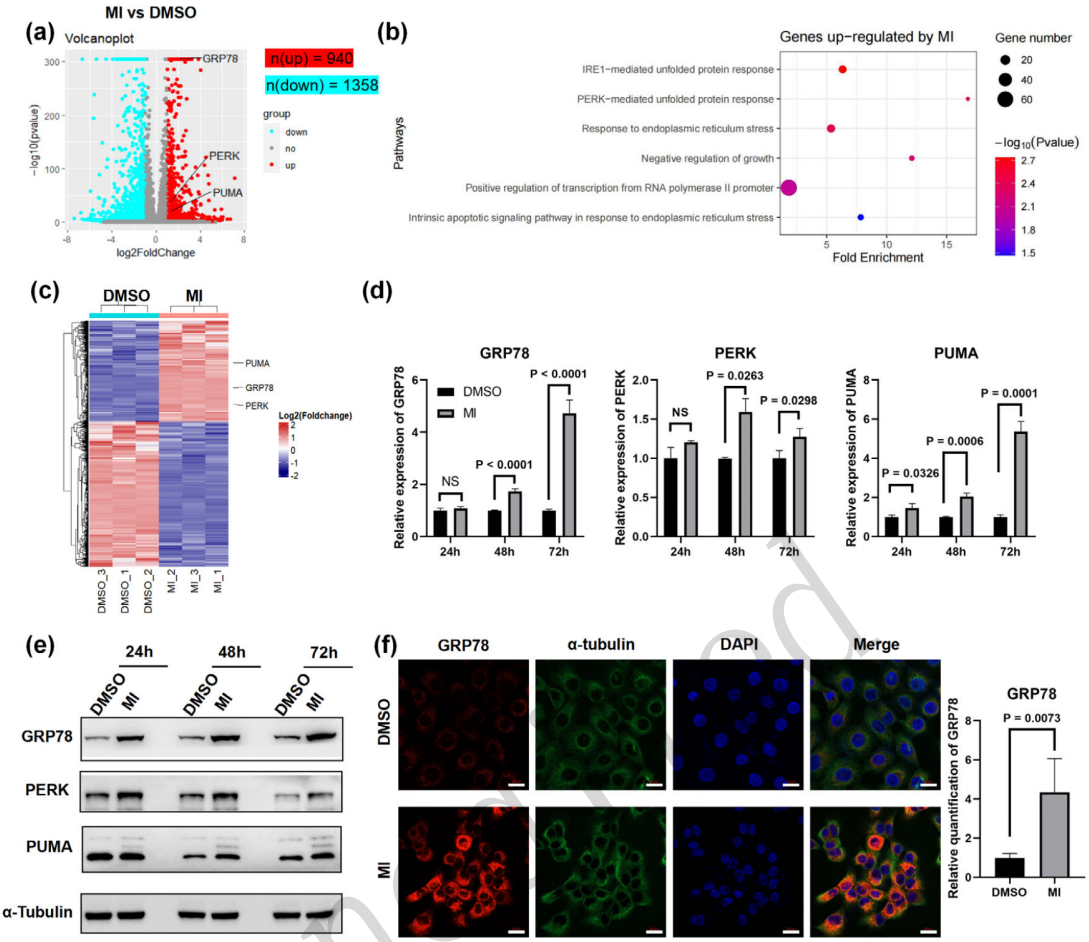

Fig. 3 MI-induced ER stress in OSCC cells. (a) The differentially expressed genes are shown in a volcano plot. RNA-seq revealed changes in the transcriptome of OSCC cell CAL27 treated with MI. With a selection criterion of P<0.05, and fold change ≥2, the results showed 2298 differentially expressed genes of OSCC cell CAL27 treated by MI (25 μM), among which 940 were upregulated and 1358 were downregulated. (b) GO analysis showed differentially expressed genes were enriched in pathways associated with ER stress. (c) Differentially expressed genes shown in a heatmap. (d) RT-qPCR showed that the ER stress markers GRP78, PERK, and PUMA were upregulated in CAL27 cells treated with MI (25 μM). Data are represented as mean±standard deviation (SD), n=3. (e) Western blotting showed that the ER stress markers GRP78, PERK, and PUMA were upregulated in CAL27 cells treated with MI (25 μM). (f) Immunofluorescence images showed that the ER stress marker, GRP78, was upregulated in CAL27 cells treated with MI (25 μM). The scale bar represents 20 μm. The left bar chart represents quantitative data of GRP78 in immunofluorescence images. Data are represented as mean±standard deviation (SD), n=3.

3.4 The ribosomal proteins identified as direct targets of MI

Functional in vitro and in vivo experiments showed that MI plays an anticancer role in OSCC. RNA-seq results suggested that MI induced ER stress in OSCC cells. However, we sought to identify the direct protein targets of MI. CETSA is a robust method used in biochemistry and drug discovery to assess the binding of drugs to target proteins within living cells. This assay is based on the biophysical principle that ligand binding enhances the thermal stability of the target protein and was first described by scientists in 2013 (Martinez Molina et al., 2013). We used the CETSA method to investigate the direct targets of MI. Recently, an increasing number of studies have used CETSA in conjunction with mass spectrometry (MS) or western blotting (WB) to explore or confirm the direct target of a drug.

Numerous CETSA studies have indicated that around 50 °C is a suitable temperature for experimental conditions. We performed CETSA experiments at 40, 45, 50, 55, and 60 °C, using silver staining to assess

protein thermal denaturation in CAL27 cells. Silver staining showed that proteins began to denature significantly above 50 °C (Fig. S5). Therefore, we chose 50 °C as the CETSA experimental condition for MS analysis. CAL27 cells treated with MI (MI group) served as the experimental group, while cells treated with DMSO (DMSO group) were the control group. CETSA samples from MI and DMSO groups were prepared for MS analysis and samples from each groups were analyzed in triplicate. According to the CETSA theory, small-molecule compounds can enhance the thermal stability of proteins upon binding. Thus, MI stabilizes its direct binding proteins against thermal denaturation. Proteins with increased concentration in the MI group compared to the control group were likely direct MI-binding proteins. We selected proteins with a >10% increased concentration in the experimental group from each MS result. We then identified proteins consistently showing a >10% concentration increase across all three MS results. A total of 61 differentially expressed proteins were identified. DBSCAN clustering analysis revealed that these 61 upregulated proteins were mainly ribosomal proteins, including RPL7, RPL11, RPL12, RPL18, RPL30, RPL38, RPS13, and RPS25 (Figs. 4a and 4b). GO analysis showed that the 61 upregulated proteins were enriched in ribosomes and involved in cytoplasmic translation, the primary function of ribosomes (Figs. 4c and 4d).

We acquired commercially available ribosomal proteins (RPL11, RPL38, RPL12, and RPS13) to characterize their binding affinity with MI using surface plasmon resonance (SPR). The measured dissociation constants (KD) were 5.76×10^{-6} M for RPL11 (Fig. 4e), 1.22×10^{-5} M for RPL38 (Fig. 4f), 4.25×10^{-6} M for RPL12 (Fig. S6a), and 1.21×10^{-5} M for RPS13 (Fig. S6b), indicating moderate interaction strengths between these ribosomal proteins and MI.

unedited

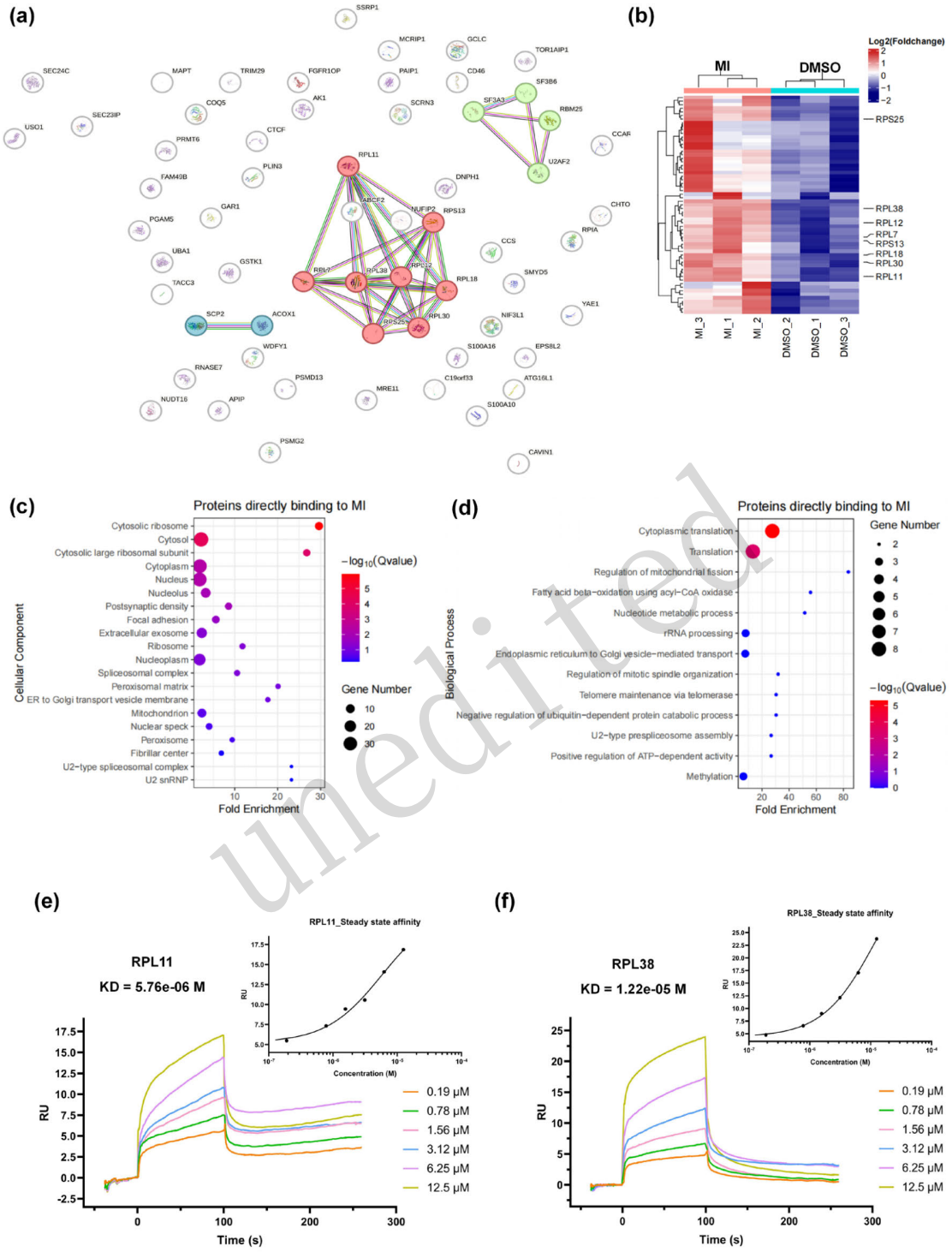

unedited

Fig. 4 CETSA and SPR results showing that MI probably interacts directly with ribosomal proteins in OSCC. (a) In the three CETSA experiments conducted for MI in OSCC CAL27 cells, 61 proteins exhibited over a 10% increase in expression. These proteins were subsequently analyzed using DBSCAN clustering through the STRING database. The outcomes predominantly indicated clustering around ribosomal proteins (RPL7, RPL11, RPL12, RPL18, RPL30, RPL38, RPS13, RPS25). (b) A heatmap showing 61 upregulated proteins in the MI group compared with the control DMSO group in the CETSA-MS experiment. Ribosomal proteins (RPL7, RPL11, RPL12, RPL18, RPL30, RPL38, RPS13, RPS25) are annotated on the right side of the heatmap. (c) GO analysis revealed that the 61 upregulated proteins from the CETSA ex-

periments conducted for MI accumulated mainly in the cellular component, 'cytosolic ribosome'. (d) The 61 upregulated proteins from the CETSA experiments conducted for MI were found to participate mainly in cytoplasmic translation, the main function of ribosomes. (e) SPR results showing the interaction of RPL11 with MI. In the main plot, the x-axis represents time (s) and the y-axis represents response units (RU). Curves correspond to different analyte concentrations, showing association and dissociation phases. The top-right inset shows steady-state affinity analysis with the concentration (M) as the x-axis and RU as the y-axis. For RPL11, KD = 5.76×10^{-6} M. (f) SPR results showing the interaction of RPL38 with MI. For RPL38, KD = 1.22×10^{-5} M.

The CETSA-MS results, as suggested by DBSCAN clustering analysis and GO analysis, indicated that the ribosomal proteins RPL7, RPL11, RPL12, RPL18, RPL30, RPL38, RPS13, and RPS25 were the key direct targets of MI in its anticancer role. The direct interaction between MI and these ribosomal proteins was further validated by molecular docking. The docking scores of RPL38 (-5.39 kcal/mol), RPL7 (-7.02 kcal/mol), RPL11 (-6.71 kcal/mol), RPL12 (-5.96 kcal/mol), RPL18 (-6.27 kcal/mol), RPL30 (-6.20 kcal/mol), RPS13 (-6.55 kcal/mol), and RPS25 (-5.93 kcal/mol) indicate their binding potential with MI (Figs. 5a-i). These potential MI-targeting ribosomal proteins were validated by CETSA-WB. Most of them exhibited high thermal stability upon MI treatment, suggesting direct interactions with MI (Figs. 5j-q).

unedited

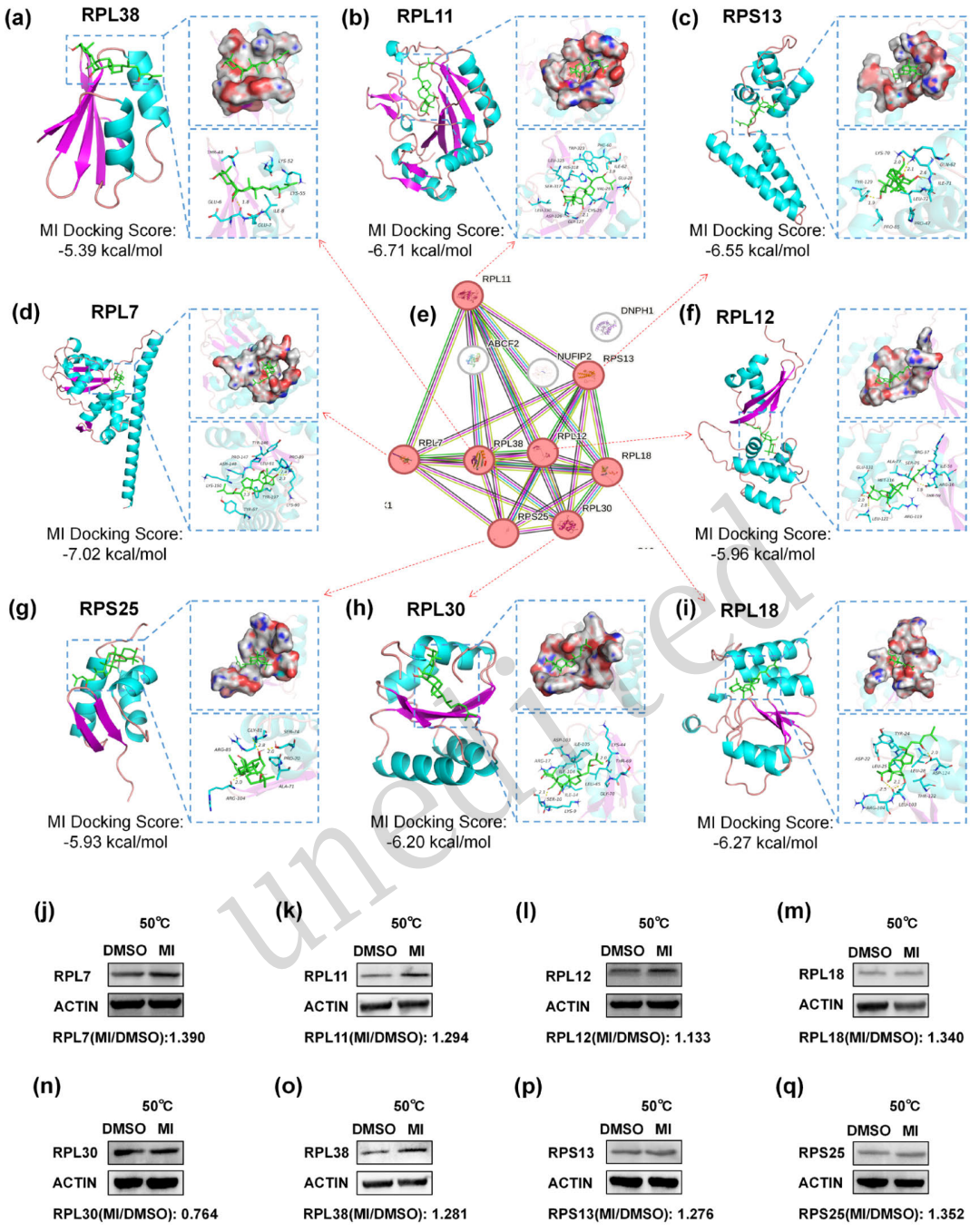

unedited

Fig. 5 The molecular docking results of ribosomal proteins found to bind directly to MI in the OSCC CETSA experiments, validated by CETSA-WB. (a-i) Molecular docking results for MI with various ribosomal proteins, showing their predicted interactions and docking scores. MI's interactions with RPL38 (A, -5.39 kcal/mol), RPL11 (B, -6.71 kcal/mol), RPS13 (C, -6.55 kcal/mol), RPL7 (D, -7.02 kcal/mol), RPL12 (F, -5.96 kcal/mol), RPS25 (G, -5.93 kcal/mol), RPL30 (H, -6.20 kcal/mol), and RPL18 (I, -6.27 kcal/mol) are depicted. The 3D protein structures are shown alongside magnified views of the binding sites, with key interacting residues and the MI molecule highlighted in green. (e) The protein-protein interaction network of ribosomal proteins, generated from the STRING database, originally part of Fig. 4a. This network shows close interactions between these potential MI-targeting ribosomal proteins, suggesting their involvement in MI's cellular effects in OSCC CAL27 cells. (j-q) The CETSA-WB results of potential MI-targeting ribosomal proteins in CAL27 cells at 50 °C showed that the relative quantification of RPL7 (normalized to the internal control actin) in the MI group was upregulated 1.390-fold compared to the DMSO control group (J). The fold changes of other potential MI-targeting ribosomal

proteins in the MI group compared to the DMSO control group were as follows: 1.294 (RPL11), 1.133 (RPL12), 1.340 (RPL18), 0.764 (RPL30), 1.281 (RPL38), 1.276 (RPS13), and 1.352 (RPS25). Most of these potential MI-targeting ribosomal proteins exhibited high thermal stability at 50 °C upon MI treatment, suggesting direct interactions with MI.

To directly assess the causal role of ribosomal proteins in MI-induced ER stress and anti-cancer effects, we performed siRNA-mediated knockdown of *RPL7* and *RPL11* in CAL27 cells. The results showed that siRNAs *RPL7*si1 and *RPL11*si1 were most effective for *RPL7* and *RPL11* knockdown, respectively (Figs. S7a and S7b). Therefore, *RPL7*si1 and *RPL11*si1 were chosen for subsequent knockdown experiments. Crucially, western blot analysis revealed that MI-induced upregulation of the ER stress markers GRP78 and PERK was significantly attenuated in *RPL7*- or *RPL11*-knockdown cells compared to the NC (Negative Control) group (Figs. S7c and S7f), indicating their causal role in MI-induced ER stress. While knockdown of either *RPL7* or *RPL11* alone inhibited cell proliferation, consistent with their essential ribosomal function, combinatorial treatment with MI resulted in a significantly enhanced anti-proliferative effect compared to MI treatment in control cells (NC), as determined by two-way ANOVA (Figs. S7d, S7e, S7g and S7h). The enhanced inhibition upon MI treatment in *RPL7*/*RPL11*-knockdown cells indicates a dual suppression of ribosomal function (knockdown followed by MI targeting), functionally identifying RPL7 and RPL11 as targets of MI.

4 Discussion

In this study, we compared the anticancer effects of nine commercially available triterpenoid monomer compounds from bitter melon extract on CAL27 and HN4 OSCC cells through CCK8 proliferation assays, as well as Transwell migration and invasion assays. The results indicated that MI was the most effective anticancer monomer among the nine tested triterpenoid monomer compounds. This result is consistent with another recent study that highlighted the anticancer role of MI in HNSCC (Sur et al., 2021). Based on this result, we confirmed that MI from bitter melon extracts is a key monomer compound with anticancer effects. We confirmed the anticancer role of MI in vivo using subcutaneous tumor formation in nude mice. We also examined the influence of MI on the mitochondrial potential and apoptosis of OSCC cells, which had not previously been studied. Our results revealed that OSCC cells CAL27 treated with MI exhibited a loss of mitochondrial potential and an increased apoptosis rate. ER stress inhibitor TUDCA attenuated MI-induced mitochondrial membrane potential depolarization and the apoptosis rate, showing that ER stress plays a crucial role in mediating MI-induced apoptosis in OSCC cells. These findings further validated the inhibitory effects of MI on OSCC cells. Moreover, in contrast to a previous study, we investigated the detailed role of MI in OSCC at the transcriptome level using RNA-seq analysis and identified the direct target of MI through CETSA. To investigate the impact of MI on OSCC at the whole-transcriptome level, we performed RNA-seq analysis on CAL27 cells treated with or without MI. GO analysis of the upregulated genes indicated that MI induced ER stress in the OSCC cells. This was confirmed by detecting ER stress markers, such as GRP78, PERK, and PUMA. The results of RNA-seq analysis revealed that MI induced ER stress in OSCC cells. Furthermore, we conducted CETSA-MS and identified ribosomal proteins RPL7, RPL11, RPL12, RPL18, RPL30, RPL38, RPS13, and RPS25 as direct target proteins of MI. As the ribosome plays a crucial role in facilitating initial protein folding, the interaction between MI and ribosomal proteins likely disrupts the function of the ribosome during protein folding, thereby inducing an unfolded protein response (UPR) and ER stress. To directly assess the causal role of ribosomal proteins in MI-induced ER stress and anti-cancer effects, we knocked down RPL7 and RPL11 in CAL27 cells using siRNA. MI-induced upregulation of ER stress markers GRP78 and PERK was significantly attenuated in *RPL7* or *RPL11* knockdown cells, showing their causal role in MI-induced ER stress. Knocking down either *RPL7* or *RPL11* alone inhibited cell proliferation, and combinatorial treatment with MI enhanced the anti-proliferative effect. The enhanced inhibition in *RPL7*/*RPL11* knockdown cells upon MI treatment indicated dual suppression of ribosomal function, identifying RPL7 and RPL11 as MI targets. This apparent paradox—enhanced cytotoxicity yet blunted ER stress upon target knockdown—could be mechanistically explained by the compromised ribosomal function and consequent reduction in global protein synthesis caused by *RPL7* or *RPL11* depletion. While MI still targets ribosomal components in knockdown cells, the diminished protein synthesis capacity lowers the burden of misfolded proteins below the threshold required for robust ER stress activation.

Uncorrected

Altogether, MI induced ER stress and inhibited OSCC by targeting ribosomal proteins, demonstrating its potential therapeutic roles against OSCC.

Unlike in other studies on the role of MI, we conducted a CETSA experiment and identified the direct target proteins of MI. The discovery of these direct target proteins represents the most significant innovation of our study. Specifically, we discovered that certain ribosomal proteins interacted with MI. Our study is the first to perform transcriptome RNA-seq analysis of OSCC cells treated with MI. The RNA-seq results indicated that MI induced ER stress, a finding not previously reported.

MI is a promising natural compound with anticancer potential. Recently, its role in OSCC and HNC has drawn significant attention from researchers. In a previous study, the molecular mechanism underlying the anticancer activity of MI was elucidated for the first time. It was shown that MI inhibited c-Met signaling, showing the inhibitory effect of bitter melon extract on HNC and its influence on c-Met signaling (Sur, et al., 2021). Furthermore, MI has been reported to inhibit HNC growth by altering the immunosuppressive effects of tumor-infiltrating macrophages and B lymphocytes (Sur, et al., 2024). That study underscored the anticancer effects of MI through immune regulation, an aspect that was not considered in our study. Investigating the anticancer effects of MI from an immune regulation perspective would be a valuable area for future research.

In our study, we explored the molecular mechanism of MI in OSCC inhibition through transcriptome RNA-seq analysis and CETSA-MS. We discovered that MI targets ribosomal proteins (RPL7, RPL11, RPL12, RPL18, RPL30, RPL38, RPS13, and RPS25), thereby inducing ER stress in OSCC cells. These findings highlight MI's unique mechanistic pathways in OSCC, distinct from its previously reported roles in HNC. Specifically, while Sur, et al. (2021) validated MI's anticancer effects in HNC through mechanistic studies of bitter melon extract (Sur, et al., 2021), our work identified MI's direct ribosomal protein targeting as a novel mechanism in OSCC. Although our multi-methodological approach provides robust evidence, MI may exhibit additional anticancer mechanisms in OSCC that warrant further investigation.

Lee et al. (2022) used microwave- and ultrasound-assisted extraction (MAE/UAE) to identify MI as a primary cucurbitane-type triterpenoid in bitter melon and showed its antiproliferative effects on the OSCC cell line SAS. While this work pioneered the direct extraction of cucurbitane-type triterpenoids from natural sources, it did not explore the molecular mechanisms behind MI's anti-OSCC activity. Our approach differed by using commercially sourced triterpenoids rather than performing direct extractions. This strategic choice allowed us to systematically investigate MI's unique mechanism of action in OSCC inhibition, particularly through ribosomal protein targeting and ER stress induction.

We discovered various molecular mechanisms underlying the role of MI in OSCC. Beyond its anticancer effects, Li et al. (2023) demonstrated that MI could suppress PLA2G6 and DGK-ζ, thereby alleviating isoproterenol-induced cardiomyocyte hypertrophy, which further supports the concept of MI's multifaceted mechanisms of action. Additionally, Chen et al. (2018) revealed that MI inhibits high-glucose-induced fibroblast activation by activating nuclear factor erythroid 2-related factor 2 (Nrf2) (Chen et al., 2018a). These findings collectively highlight MI as a multifaceted compound with cross-disease mechanistic versatility.

In our study, we discovered that MI induces ER stress, a phenomenon not previously reported in any other MI study. Numerous studies have highlighted the role of ER stress in OSCC inhibition. Additionally, She et al. (2022) reported that 4-carbomethoxyl-10-epigyrosanoldie E, derived from the cultured soft coral *Sinularia sandensis*, induced apoptosis and autophagy through ROS and mitochondrial dysfunction as well as ER stress in OSCC. Hsu, et al. (2022) showed that Z-ligustilide induces c-Myc-dependent apoptosis by activating ER stress signaling in OSCC, which also enhances the radiosensitivity of OSCC cells (Hsu, et al., 2022). Cantharidin induces ER stress and inhibits OSCC proliferation (Xi et al., 2015).

In our study, we identified ribosomal proteins RPL7, RPL11, RPL12, RPL18, RPL30, RPL38, RPS13, and RPS25 as direct targets of MI for the first time. Ribosomes are not only the primary sites of translation but also function as crucial organelles in protein folding (Kaiser et al., 2011; Holtkamp et al., 2015; Liu et al., 2019; Waudby et al., 2019; Ahn et al., 2022; Wales et al., 2024). For instance, RPL12 can affect the folding of the CFTR protein (Oliver et al., 2019). RPL26 UFMylation enables the degradation of stalled nascent chains and promotes the targeting of translocation-arrested ER proteins to lysosomes for degradation, thereby preventing misfolded protein accumulation and restoring ER proteostasis (Wang et al., 2020). Protein biosynthesis is closely linked to co-translational folding, which initiates during synthesis. This process is regulated by both the ribosomal exit tunnel architecture and intramolecular polypeptide interactions. As nascent polypeptides emerge from the tunnel, they undergo hierarchical structural transitions to attain native conformations (Wruck et al.,

Uncorrected

2017). Cellular functionality relies on proteome integrity, which necessitates precise regulation of protein synthesis and folding fidelity. Ribosomes act as central hubs for mRNA quality control and nascent chain surveillance, ensuring error-free translation and proper protein maturation (Alagar Boopathy et al., 2023).
Ribosomal proteins can influence the protein folding capacity of the ER, thereby affecting the ER stress response. Dysfunctional ribosomal proteins may lead to misfolded protein accumulation in the ER, triggering ER stress. For instance, the anticancer metallodrug BOLD-100/KP1339 directly interacts with ribosomal proteins RPL10 and RPL24, leading to ER stress and proliferation inhibition (Neuditschko et al., 2021). The ER stress sensor IRE1α interacts with specific ribosomal proteins (RPL9, RPL10A, RPS14, RPS24), indicating a close association between ribosomes and ER stress (Acosta-Alvear et al., 2018). We propose that MI, by targeting ribosomal proteins (RPL7, RPL11, RPL12, RPL18, RPL30, RPL38, RPS13, RPS25), disrupts ribosomal function. This interference likely impairs the protein folding capacity of ribosomes, resulting in misfolded protein accumulation—a primary driver of ER stress. Persistent ER stress ultimately activates pro-apoptotic pathways, thereby exerting inhibitory effects on OSCC.

Ribosomal proteins have been shown to play critical roles in cancer development and progression. Ribosomal protein L11 (RPL11) directly interacts with MDM2, inhibiting its ubiquitin ligase activity and blocking MDM2-mediated p53 ubiquitination and degradation (Zhang et al., 2003; Sasaki et al., 2011; Ichikawa and Saitoh, 2022). Impaired ribosome biogenesis activates the p53-dependent nucleolar stress response, leading to cell cycle arrest—a conserved surveillance mechanism implicated in cancer and ribosomopathies (Fumagalli et al., 2012). RPL38 promotes gastric cancer cell proliferation and invasion while suppressing apoptosis (Ji and Zhang, 2020). Ribosomal protein S13 drives gastric cancer progression through p27 downregulation and confers multidrug resistance by inhibiting drug-induced apoptosis (Shi et al., 2004; Guo et al., 2011). RPS25 interacts with MDM2 to inhibit its E3 ligase activity, thereby stabilizing p53 and enhancing its tumor-suppressive function (Zhang et al., 2013).

In this study, we found that MI induces ER stress and plays a role in inhibiting OSCC. We further identified eight ribosomal proteins that directly interact with MI. Ribosomes are organelles that play crucial roles in cells. They are responsible for protein translation and play a significant role in the initial folding of proteins. MI targets multiple ribosomal proteins, which may interfere with the normal functioning of the ribosomes. This could potentially be the mechanism by which MI induces ER stress and inhibits OSCC (Fig. 6). Based on these findings, we hypothesize that MI affects the normal function of ribosomes during protein folding, thereby causing ER stress. However, we did not further explore the individual roles of the eight ribosomal proteins directly interacting with MI in OSCC.

unedited

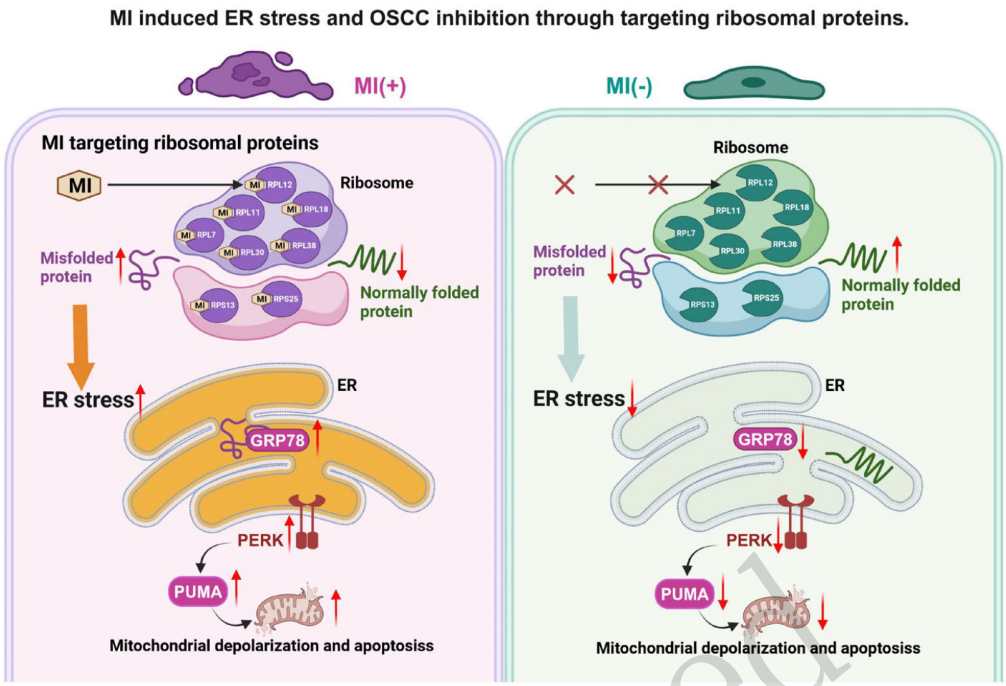

Fig. 6 MI induces ER stress and OSCC inhibition by targeting ribosomal proteins. MI targets and interferes with multiple ribosomal proteins (RPL7, RPL11, RPL12, RPL18, RPL30, RPL38, RPS13, and RPS25) in the ribosome, leading to the production of misfolded proteins that accumulate and cause endoplasmic reticulum (ER) stress and OSCC inhibition. This figure was created with BioRender.com.

Drugs often act on multiple targets to achieve their therapeutic effects, and MI is no exception. As an active ingredient of the natural compound found in bitter melon, MI is increasingly attracting the attention of researchers worldwide, and its various roles in OSCC and other fields are expected to be further elucidated. Regarding the anticancer effects of MI, further studies are needed to investigate its influence on sensitivity to radiotherapy and chemotherapy, as well as its role in tumor immunity.

unedited

5 Conclusions

MI induced ER stress and inhibited OSCC by targeting ribosomal proteins, demonstrating its potential therapeutic roles against OSCC. The identification of ribosomal proteins as direct molecular targets of MI represents the most significant innovation of this study. While we have characterized the functional contributions of RPL7 and RPL11 in MI-induced ER stress and OSCC suppression, future investigations will focus on a more systematic exploration of all identified ribosomal protein targets.

Data availability statement

All datasets analyzed in this study are available from the authors upon request.

Acknowledgments

This work was supported by the National Natural Science Foundation of China (Grant No. 82203404 to J.L.K.), the Zhejiang Provincial Pioneer Goose + X Program (Grant No. 2025C02101 to Y.L.), and the Zhejiang Provincial Natural Science Foundation (Grant No. LQ21H140002 to Y.L.).

I would like to express my sincere gratitude to Professor Honghe Zhang and Dr. Yinli Zhang for their assistance during the writing process of this article.

Author contributions

Jianlu KONG contributed to the experiments operation, data analysis, manuscript drafting, and funding. Ziyu ZHU contributed to the experiments operation, literature review, and data collection. Yijie HU contributed to the experiments operation and literature review. Siyi ZHOU contributed to the experiments operation and data collection. Tianyi GU contributed to the experiments operation. Xiao SHEN contributed to the literature review. Huiming WANG and Mengfei YU contributed to the supervision and editing. Yu LIU contributed to the supervision and funding.

Compliance with ethics guidelines

The authors Jianlu KONG, Ziyu ZHU, Yijie HU, Siyi ZHOU, Tianyi GU, Xiao SHEN, Huiming WANG, Mengfei YU, and Yu LIU declare that they have no known competing financial interests or personal relationships that could have influenced the work reported in this study.

Animal experiments were performed in accordance with the protocol approved by the Animal Care and Use Committee of Zhejiang University (ETHICS CODE: ZJU20210268). All institutional and national guidelines for the care and use of laboratory animals were followed.

References

Acosta-Alvear D, Karagöz GE, Fröhlich F, et al., 2018. The unfolded protein response and endoplasmic reticulum protein targeting machineries converge on the stress sensor ire1. *Elife*, 7 https://doi.org/10.7554/eLife.43036

Ahn M, Włodarski T, Mitropoulou A, et al., 2022. Modulating co-translational protein folding by rational design and ribosome engineering. *Nat Commun*, 13(1):4243. https://doi.org/10.1038/s41467-022-31906-z

Alagar Boopathy LR, Beadle E, Garcia-Bueno Rico A, et al., 2023. Proteostasis regulation through ribosome quality control and no-go-decay. *Wiley Interdiscip Rev RNA*, 14(6):e1809. https://doi.org/10.1002/wrna.1809

Bai LY, Chiu CF, Chu PC, et al., 2016. A triterpenoid from wild bitter gourd inhibits breast cancer cells. *Sci Rep*, 6:22419. https://doi.org/10.1038/srep22419

Blot WJ, Mclaughlin JK, Winn DM, et al., 1988. Smoking and drinking in relation to oral and pharyngeal cancer. *Cancer Res*, 48(11):3282-3287.

Bray F, Ferlay J, Soerjomataram I, et al., 2018. Global cancer statistics 2018: Globocan estimates of incidence and mortality worldwide for 36 cancers in 185 countries. *CA Cancer J Clin*, 68(6):394-424. https://doi.org/10.3322/caac.21492

Chen F, Huang G, Huang H, 2021. Preparation, analysis, antioxidant activities in vivo of phosphorylated polysaccharide from momordica charantia. *Carbohydr Polym*, 252:117179. https://doi.org/10.1016/j.carbpol.2020.117179

Chen PY, Shih NL, Hao WR, et al., 2018a. Inhibitory effects of momordicine i on high-glucose-induced cell proliferation and collagen synthesis in rat cardiac fibroblasts. *Oxid Med Cell Longev*, 2018:3939714. https://doi.org/10.1155/2018/3939714

Chen SW, Zhang Q, Guo ZM, et al., 2018b. Trends in clinical features and survival of oral cavity cancer: Fifty years of experience with 3,362 consecutive cases from a single institution. *Cancer Manag Res*, 10:4523-4535. https://doi.org/10.2147/cmar.S171251

Chen YJ, Chang JT, Liao CT, et al., 2008. Head and neck cancer in the betel quid chewing area: Recent advances in molecular carcinogenesis. *Cancer Sci*, 99(8):1507-1514. https://doi.org/10.1111/j.1349-7006.2008.00863.x

Dai Y, Wu Z, Chen Y, et al., 2023. Oct4's role and mechanism underlying oral squamous cell carcinoma. *J Zhejiang Univ Sci B*, 24(9):796-806. https://doi.org/10.1631/jzus.B2200602

Feller LL, Khammissa RR, Kramer BB, et al., 2013. Oral squamous cell carcinoma in relation to field precancerisation: Pathobiology. *Cancer Cell Int*, 13(1):31. https://doi.org/10.1186/1475-2867-13-31

Fumagalli S, Ivanenkov VV, Teng T, et al., 2012. Suprainduction of p53 by disruption of 40s and 60s ribosome biogenesis leads to the activation of a novel g2/m checkpoint. *Genes Dev*, 26(10):1028-1040. https://doi.org/10.1101/gad.189951.112

Gao P, Zhang W, Lin Y, et al., 2023. Luteolin suppresses oral carcinoma 3 (oc3) cell growth and migration via modulating polo-like kinase 1 (plk1) expression and cellular energy metabolism. *J Zhejiang Univ Sci B*, 24(12):1151-1158. https://doi.org/10.1631/jzus.B2300200

Guo X, Shi Y, Gou Y, et al., 2011. Human ribosomal protein s13 promotes gastric cancer growth through down-regulating p27(kip1). *J Cell Mol Med*, 15(2):296-306. https://doi.org/10.1111/j.1582-4934.2009.00969.x

Hennessey PT, Westra WH, Califano JA, 2009. Human papillomavirus and head and neck squamous cell carcinoma:

Unedited

Recent evidence and clinical implications. *J Dent Res*, 88(4):300-306. https://doi.org/10.1177/0022034509333371

Holtkamp W, Kokic G, Jäger M, et al., 2015. Cotranslational protein folding on the ribosome monitored in real time. *Science*, 350(6264):1104-1107. https://doi.org/10.1126/science.aad0344

Hsu RJ, Peng KY, Hsu WL, et al., 2022. Z-ligustilide induces c-myc-dependent apoptosis via activation of er-stress signaling in hypoxic oral cancer cells. *Front Oncol*, 12:824043. https://doi.org/10.3389/fonc.2022.824043

Ichikawa MK, Saitoh M, 2022. Direct and indirect roles of grwd1 in the inactivation of p53 in cancer. *J Biochem*, 171(6):601-603. https://doi.org/10.1093/jb/mvac010

Ji H, Zhang X, 2020. Rpl38 regulates the proliferation and apoptosis of gastric cancer via mir-374b-5p/vegf signal pathway. *Onco Targets Ther*, 13:6131-6141. https://doi.org/10.2147/ott.S252045

Kaiser CM, Goldman DH, Chodera JD, et al., 2011. The ribosome modulates nascent protein folding. *Science*, 334(6063):1723-1727. https://doi.org/10.1126/science.1209740

Kao Y, Chou CH, Huang LC, et al., 2023. Momordicine i suppresses glioma growth by promoting apoptosis and impairing mitochondrial oxidative phosphorylation. *Excli j*, 22:482-498. https://doi.org/10.17179/excli2023-6129

Lee YT, Pao LH, Chen CY, et al., 2022. Microwave- and ultrasound-assisted extraction of cucurbitane-type triterpenoids from momordica charantia l. Cultivars and their antiproliferative effect on sas human oral cancer cells. *Foods*, 11(5) https://doi.org/10.3390/foods11050729

Liu K, Maciuba K, Kaiser CM, 2019. The ribosome cooperates with a chaperone to guide multi-domain protein folding. *Mol Cell*, 74(2):310-319.e317. https://doi.org/10.1016/j.molcel.2019.01.043

Martinez Molina D, Jafari R, Ignatushchenko M, et al., 2013. Monitoring drug target engagement in cells and tissues using the cellular thermal shift assay. *Science*, 341(6141):84-87. https://doi.org/10.1126/science.1233606

Neuditschko B, Legin AA, Baier D, et al., 2021. Interaction with ribosomal proteins accompanies stress induction of the anticancer metallodrug bold-100/kp1339 in the endoplasmic reticulum. *Angew Chem Int Ed Engl*, 60(10):5063-5068. https://doi.org/10.1002/anie.202015962

Oliver KE, Rauscher R, Mijnders M, et al., 2019. Slowing ribosome velocity restores folding and function of mutant cftr. *J Clin Invest*, 129(12):5236-5253. https://doi.org/10.1172/jci124282

Pitchakarn P, Suzuki S, Ogawa K, et al., 2012. Kuguacin j, a triterpeniod from momordica charantia leaf, modulates the progression of androgen-independent human prostate cancer cell line, pc3. *Food Chem Toxicol*, 50(3-4):840-847. https://doi.org/10.1016/j.fct.2012.01.009

Pitchakarn P, Umsumarng S, Mapoung S, et al., 2017. Kuguacin j isolated from bitter melon leaves modulates paclitaxel sensitivity in drug-resistant human ovarian cancer cells. *J Nat Med*, 71(4):693-702. https://doi.org/10.1007/s11418-017-1099-0

Sasaki M, Kawahara K, Nishio M, et al., 2011. Regulation of the mdm2-p53 pathway and tumor growth by pict1 via nucleolar rpl11. *Nat Med*, 17(8):944-951. https://doi.org/10.1038/nm.2392

She YY, Lin JJ, Su JH, et al., 2022. 4-carbomethoxyl-10-epigyrosanoldie e extracted from cultured soft coral sinularia sandensis induced apoptosis and autophagy via ros and mitochondrial dysfunction and er stress in oral cancer cells. *Oxid Med Cell Longev*, 2022:3017807. https://doi.org/10.1155/2022/3017807

Shi Y, Zhai H, Wang X, et al., 2004. Ribosomal proteins s13 and l23 promote multidrug resistance in gastric cancer cells by suppressing drug-induced apoptosis. *Exp Cell Res*, 296(2):337-346. https://doi.org/10.1016/j.yexcr.2004.02.009

Sur S, Ray RB, 2021. Diverse roles of bitter melon (momordica charantia) in prevention of oral cancer. *J Cancer Metastasis Treat*, 7 https://doi.org/10.20517/2394-4722.2020.126

Sur S, Steele R, Isbell TS, et al., 2021. Momordicine-i, a bitter melon bioactive metabolite, displays anti-tumor activity in head and neck cancer involving c-met and downstream signaling. *Cancers (Basel)*, 13(6) https://doi.org/10.3390/cancers13061432

Sur S, Bhartiya P, Steele R, et al., 2024. Momordicine-i suppresses head and neck cancer growth by reprogrammimg immunosuppressive effect of the tumor-infiltrating macrophages and b lymphocytes. *Mol Cancer Ther*, https://doi.org/10.1158/1535-7163.Mct-23-0718

Wales TE, Pajak A, Roeselová A, et al., 2024. Resolving chaperone-assisted protein folding on the ribosome at the peptide level. *Nat Struct Mol Biol*, https://doi.org/10.1038/s41594-024-01355-x

Wang H, Khor TO, Shu L, et al., 2012. Plants vs. Cancer: A review on natural phytochemicals in preventing and treating cancers and their druggability. *Anticancer Agents Med Chem*, 12(10):1281-1305. https://doi.org/10.2174/187152012803833026

Wang L, Xu Y, Rogers H, et al., 2020. Ufmylation of rpl26 links translocation-associated quality control to endoplasmic reticulum protein homeostasis. *Cell Res*, 30(1):5-20. https://doi.org/10.1038/s41422-019-0236-6

Journal Pre-proof

Waudby CA, Dobson CM, Christodoulou J, 2019. Nature and regulation of protein folding on the ribosome. *Trends Biochem Sci*, 44(11):914-926. https://doi.org/10.1016/j.tibs.2019.06.008

Wruck F, Katranidis A, Nierhaus KH, et al., 2017. Translation and folding of single proteins in real time. *Proc Natl Acad Sci U S A*, 114(22):E4399-e4407. https://doi.org/10.1073/pnas.1617873114

Xi Y, Garshott DM, Brownell AL, et al., 2015. Cantharidins induce er stress and a terminal unfolded protein response in oscc. *J Dent Res*, 94(2):320-329. https://doi.org/10.1177/0022034514559376

Yang M, Luo Q, Chen X, et al., 2021. Bitter melon derived extracellular vesicles enhance the therapeutic effects and reduce the drug resistance of 5-fluorouracil on oral squamous cell carcinoma. *J Nanobiotechnology*, 19(1):259. https://doi.org/10.1186/s12951-021-00995-1

Yue J, Sun Y, Xu J, et al., 2019. Cucurbitane triterpenoids from the fruit of momordica charantia l. And their anti-hepatic fibrosis and anti-hepatoma activities. *Phytochemistry*, 157:21-27. https://doi.org/10.1016/j.phytochem.2018.10.009

Zhang X, Wang W, Wang H, et al., 2013. Identification of ribosomal protein s25 (rps25)-mdm2-p53 regulatory feedback loop. *Oncogene*, 32(22):2782-2791. https://doi.org/10.1038/onc.2012.289

Zhang Y, Wolf GW, Bhat K, et al., 2003. Ribosomal protein l11 negatively regulates oncoprotein mdm2 and mediates a p53-dependent ribosomal-stress checkpoint pathway. *Mol Cell Biol*, 23(23):8902-8912. https://doi.org/10.1128/mcb.23.23.8902-8912.2003

Supplementary information

Tables S1-S3; Figs. S1-S7

unedited